Rotor aerodynamic interference of aerial-aquatic vehicles in free water surface effect

Qi ZHAN[1], Yumin YANG[2], Shuai ZHAO[1], Yousong XU[1], Xiao WANG[1,*], Junhui HU[2,*]

National Key Laboratory of Helicopter Aeromechanics, Nanjing University of Aeronautics and Astronautics, Nanjing 210016, China

State Key Laboratory of Mechanics and Control for Aerospace Structures, Nanjing University of Aeronautics and Astronautics, Nanjing 210016, China

Abstract

In recent years, aerial-aquatic rotorcraft that operate across multiple mediums have attracted considerable attention from researchers due to their unique flight capabilities. However, when rotorcraft traverse different media or operate near the water surface, they are required to overcome aerodynamic interference caused by the complex gas-liquid multiphase flow field. This reduces the confidence of aerodynamic performance evaluation models used in the design process, as well as the robustness of control systems designed based on these aerodynamic models, leading to failures in vehicle traversal or decreased hovering stability. In this study, the Lattice-Boltzmann method and turbulence model based large-eddy simulation method were employed to investigate the aerodynamic interference characteristics of isolated rotors and parallel multi-rotors near the water surface. Subsequently, a near-water surface/ground experimental system was established to compare and validate the effectiveness and computational accuracy of the numerical simulation models. The study found that the depression region caused by the deformation of the water surface obstructs the diffusion of the rotor wake, leading the isolated rotor to temporarily enter a vortex ring state, resulting in aerodynamic losses. Compared to the traditional ground effect, the thrust enhancement effect of the wall effect under the influence of gas-liquid coupling is suppressed, and may even be lower than the thrust without ground effect. Unlike isolated rotors, the thrust reduction caused by the free-water surface effect can be effectively mitigated by controlling the inter-rotor spacing of parallel multi-rotors. However, the cost of this mitigation is that the gas-liquid coupling effects increase the disorder in the flow field, exacerbating the imbalance in the aerodynamic force distribution across the rotor plane.

1. NOTATION

Symbols

R	Rotor radius, m
c	Blade chord length
C_T	Thrust coefficient
C_p	Pressure coefficient
ω	Rotor speed of rotation, RPM
ϕ	Vortex age
T_{tt}	Time for a rotor revolution
ρ_a	Air density
h	Distance from rotor plane to surface

Acronyms:

AAR	Aerial-Aquatic Rotorcraft
CFD	Computational Fluid Dynamics
FVM	Finite Volume Method
LBM	Lattice Boltzmann Method
LES	Large-Eddy Simulation
GE	Ground Effect
FWSE	Free Water Surface Effect

2. INTRODUCTION

In recent years, the rapid advancement of aerial-aquatic rotorcraft (AAR)—systems capable of executing both aerial and underwater missions—has garnered significant attention across civilian and military sectors, as discussed in Ref. 1–3. By integrating the underwater stealth capabilities of submersibles with the agility and mobility of aerial platforms, AAR provide a versatile solution for multi-domain operations across distinct environments.

AAR must perform rapid and seamless transitions between air and water, posing substantial challenges in control design, propulsion strategy, and aerodynamic modeling, as discussed by Yi (Ref. 4), Villegas (Ref. 5), and Bi (Ref. 6). When operating near ground or water surfaces, the rotor downwash is impeded and redirected along the interface, resulting in increased pressure beneath the rotor and augmented thrust under constant power conditions. As the rotor approaches the free water surface, the downwash induces surface deformation, disrupting surface tension and generating a highly dynamic gas-liquid interaction region, as identified by Bai (Ref. 7). The interaction creates a complex multiphase flow field, characterized by strong coupling and wake vortex dynamics, which requires high-fidelity aerodynamic modeling to ensure reliable control and structural safety during the transitional stages, as discussed by Wei (Ref. 8).

Rotor aerodynamics has traditionally been analyzed using theoretical models, physical experiments, and computational fluid dynamics (CFD) simulations, as discussed in Ref. 2. While theoretical methods offer simplified insights, they often struggle to represent the nonlinear wake structures and gas-liquid interface dynamics. Similarly, while experimental techniques can capture flow behavior under controlled conditions, they are limited in resolving transient gas-liquid coupling mechanisms due to interface deformation, interference from droplet reflection, and spatial resolution limitations, as discussed by Bai et al. in Ref. 9. The inherent complexity of multiphase flows—which involves strongly coupled momentum, pressure, and interface dynamics—makes experimental approaches insufficient and costly. Furthermore, CFD methods, particularly those based on the Navier–Stokes equations combined with the finite volume method (FVM), have become the dominant framework for aerodynamic simulations. Among these, the volume of Fluid (VOF) method, introduced by Hirt and Nichols (Ref. 10) in 1981, is widely used for interface tracking via phase fraction transport in multiphase simulations. However, traditional VOF-based models are highly sensitive to grid quality, suffer from interface smearing, and often encounter difficulties in preserving surface sharpness and curvature under large interface deformations, as discussed by Chen, Wang and Li (Ref. 11–13).

To address the limitations of conventional CFD methods in simulating multiphase flows with strong interfacial dynamics, the lattice Boltzmann method (LBM) has emerged as a promising alternative, as discussed by Kumar (Ref. 14). As a mesoscopic approach based on discrete particle distribution functions, LBM naturally accommodates complex boundary conditions, strong interface deformation, and parallel computation, making it highly suitable for simulating unsteady, multi-physics environments, such as rotor–water multiphase interactions. Several LBM-based multiphase models have been proposed, each with specific advantages and drawbacks. The color-gradient model, proposed by Rothman and Keller in Ref. 15, effectively captures sharp interfaces but becomes unstable under high density and viscosity ratios. The free-energy model, derived from thermodynamic theory by Swift in Ref. 16, accurately handles interface curvature but suffers from numerical instability in geometrically complex regions. The phase-field model, proposed by He et al. in Ref. 17, offers smooth interface transitions and theoretical rigor but is computationally intensive and highly sensitive to parameter tuning. In contrast, the pseudo-potential model, proposed by Shan–Chen in Ref. 18, provides an optimal balance between computational efficiency and physical fidelity. It introduces non-local interactions to simulate surface tension and phase segregation without the need for explicit interface tracking. Its robustness and simplicity have led to its widespread adoption in multiphase simulations, especially in cases involving high density ratios and surface deformation.

In this study, a hybrid CFD framework is adopted, integrating LBM with the Shan–Chen pseudo-potential model and large-eddy simulation (LES) turbulence model to analyze the aerodynamic interference of rotors near a free water surface. Rotor wake flow visualization experiments are first conducted to qualitatively observe the surface interaction effects. Subsequently, the proposed numerical approach is employed to simulate the evolution of vortex structures and interface dynamics, enabling the analysis of the gas–liquid multiphase coupling mechanism in the proximity of a deformable free surface.

3. NUMERICAL METHODOLOGY

3.1. Governing equations

The governing equations in this study are derived from the LBM, which is used to solve the fluid dynamics in the vicinity of a rotor interacting with the free water surface. The LBM operates on the Boltzmann equation in Ref. 19, which is expressed in terms of the distribution function as follows:

$$\frac{\partial f_i}{\partial t} + \boldsymbol{v}_i \bullet \nabla f_i + F_t \bullet \nabla_v f_i = \xi(f) \quad (1)$$

where $f_i(x, t)$ is the particle distribution function at position x and time t, for the i_{th} direction. $\boldsymbol{v}_i$ is the particle velocity in the i_{th} direction. $\xi(f)$ is the collision operator that describes the particle interactions. F_t is the total body force, which can be expanded as:

$$F_t = F_e + F_i + F_s \quad (2)$$

where F_s is the solid–fluid interaction force, F_i is the interaction force among particles and F_e represents external force such as gravitational force.

The collision operator is typically modeled using the multiple relaxation time (MRT) model (in Ref. 20), which improves the stability and accuracy of the simulation by relaxing the distribution function toward an equilibrium state. The MRT collision operator can be expressed as:

$$\xi(f) = -\sum_j M_{ij}^{-1} S_{ij} M_{ij} (f^k(x,t) - f^{eq,k}(x,t)) \quad (3)$$

where M_{ij} is the transformation matrix that relates the distribution function to the moments. S_{ij} is the diagonal relaxation matrix for the different moments of the distribution. $f^{eq,k}(x, t)$ is the equilibrium distribution function, which depends on the macroscopic fluid properties such as velocity and density. The equilibrium distribution is derived from the Maxwell-Boltzmann distribution.

3.2. Boundary conditions

To model the turbulence in the flow, the LES model is incorporated into the Lattice Boltzmann framework, which has been validated by Haussmann in Ref. 21. The large-scale turbulent eddies are directly resolved while the subgrid-scale eddies through a turbulent viscosity υ_{sb}. The effective viscosity is given by

$$\upsilon_e = \upsilon_k + \upsilon_{sb} \quad (4)$$

where υ_k is the kinematic viscosity of the fluid.

The subgrid-scale viscosity is defined as,

$$\upsilon_{sb} = (C_s \Delta_g)^2 \sqrt{2 \bar{S}_{\alpha\beta} \bar{S}_{\alpha\beta}} \quad (5)$$

where, C_s is Smagorinsky–Lilly coefficient. Δ_g is the grid filter. $\bar{S}_{\alpha\beta}$ is the strain rate tensor of the resolved scales. The wall function, as proposed by shih (Ref. 22), is used to model the near-wall region and boundary layer, establishing an instantaneous relationship between wall shear stress and velocity.

For the multiphase flow, Shan-Chen pseudo-potential model (in Ref. 18) is used to simulate the gas-liquid interface. In this model, non-local interactions are introduced between fluid particles to account for surface tension and phase segregation effects without requiring explicit interface tracking. The Shan-Chen model uses the following expression for the inter-particle potential:

$$F(x,t) = -g\psi(x) \sum_i w_i \psi(x + e_i \Delta t) e_i \quad (6)$$

where g indicates the parameter which controls interaction strength. If g > 0, then the interaction force will be repulsive or attractive (g < 0), respectively. w_i is the weight factor for the i_{th} particle direction. $\Psi(\text{x})$ is the effective mass which depends on the local density estimated by the following relation (in Ref. 23):

$$\psi = \sqrt{\frac{2}{g{c_s}^2}(p - \rho {c_s}^2)} \quad (7)$$

In this study, the Carnahan-Starling equation of state (in Ref. 24), which has been widely used in large-density multiphase simulations, is adopted and expressed as follows,

$$p = \rho R_c T \frac{1 + b\rho/4 + (b\rho/4)^2 - (b\rho/4)^3}{(1 - b\rho/4)^3} - a\rho^2 \quad (8)$$

where a is the attraction parameter, b is the repulsion parameter, $a = 0.4963(R_c T_c)2/p_c$, $b = 0.1873 R_c T_c / p_c$. In this paper, $R_c = 1$, $a = 0.5$, $b = 4$. T_c and p_c are the critical temperature and pressure.

4. NUMERICAL VALIDATION

4.1. Mesh configuration

In this study, the open-source LBM code OpenLB (in Ref. 25) based on D3Q27 octree structure was employed for the numerical analysis of the gas-liquid coupling flow field. To verify the convergency and accuracy of the grid configuration and model parameters, the Caradonna-Tung (in Ref. 26) rotor with Naca0012 airfoil was used, which is shown in Figure 1.

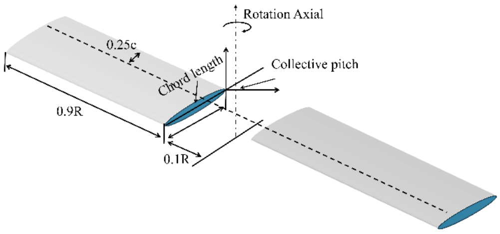

Figure 1 Rotor configuration

The primarily parameters of the rotor and environment are shown in Table 1. Based on the rotor and environmental parameters provided in Table 1, the tip speed in this study is 209.47 m/s, the tip Mach number is 0.613, and tip Reynolds number is 2.7×10^6.

Table 1 Simulation parameters

Parameters	value
Rotor radius	1.143 m
Blade chord length	0.1905 m
Rotor aspect ratio	6
Reference pressure	101325 Pa
Ambient temperature	290 K
rotational speed	1750 RPM
Collective pitch	8 deg
Air density	1.22 kg/m3
viscosity	1.8×10-5 Pa·s
Surface Tension	0.07 N/m

To reduce the number of particles and optimize computational efficiency while maintaining accuracy, a local grid refinement method is adopted, as shown in Figure 2. Figure 2(a) represents the computational domain for the C-T rotor near the ground, Figure 2(b) shows the computational domain for the rotor near the water surface, and Figure 2(c) and (d) show the grid refinement configuration. Additionally, the vertical distance from the domain boundary to the rotor's rotation center is $10R$, and a Cartesian grid is adopted.

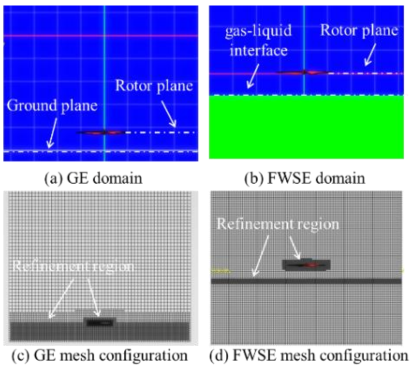

Figure 2 Mesh configuration domain for simulation

4.2. Numerical Validation

Due to the wall function and the mesoscopic nature of the LBM, grid quantity and quality are not key factors influencing the convergence accuracy of the LBM-WMLES (wall-model LES) method. However, grid independence validation remains necessary. Therefore, to ensure a sufficient boundary layer thickness and effectively capture near-wall flow characteristics, four progressively refined grid resolutions are employed. The total domain resolution scale is set to 0.02. Based on the unique structure of the LBM, the grid growth rate is fixed and is a multiple of 2. According to Schlichting's skin-friction correlation, the thickness of the first grid is set to the logarithmic layer, ensuring that y^+ ranges from 30 to 300. In the independence validation, a fixed time step is adopted, with the time step set to $1/360T_{tt}$ of the rotation period (where T_{tt} is the time for a rotor revolution). The number of grids in the entire fluid domain and the time-averaged rotor thrust coefficient over 40-50 orbital cycles are presented in Table 2. The rotor thrust coefficient (C_T) can be obtained by:

$$C_T = \frac{T}{0.5\pi\rho_a\omega^2 R^4} \tag{9}$$

where T is the rotor thrust, R is and rotor radius, and ω is the rotational speed.

As shown in Table 2, the thrust coefficient exhibits negligible changes starting from domain 3. From domain 1 to domain 3, the thrust coefficient varies by 9.43% and 3.43%, respectively. In contrast, the changes between domain 3 and domain 4 are reduced to 2.65%. Considering both numerical accuracy and computational cost, domain 3 is selected for the simulations as follow.

Table 2 Validation of the number of grids

	Δx	y^+	Number of grid	C_T
Domain 1	3.5e^{-4}	600	5.03e^{-6}	0.008788
Domain 2	8.9e^{-5}	300	7.61e^{-6}	0.009617
Domain 3	5.3e^{-5}	100	13.6e^{-6}	0.009947
Domain 4	2.7e^{-5}	30	30.2e^{-6}	0.010211

Additionally, different time steps were validated, as shown in Table 3. The time-averaged convergence coefficient ξ_T over 10 orbital cycles was used to evaluate the convergence performance of the numerical model. Ultimately, a time step of $1/360T_{tt}$ was adopted.

Table 3 Validation of the time step

	Δt	C_T	ξ_T
Domain 1	$1/120T_{tt}$	0.009917	5%
Domain 2	$1/240T_{tt}$	0.010091	3.2%
Domain 3	$1/360T_{tt}$	0.010211	1%

As shown in Figure 3, the vorticity iso-surface based on the Q-criterion shows the motion trajectory of the tip vortex. It can be seen that the attached vortex starts to contract from the rotor blade root, moves radially along the rotor towards the blade tip, and eventually detaches from the tip. The tip vortex then contracts inward, forming a spiral shape and slowly descending. Additionally, a small number of secondary vortices is generated alongside the formation of the tip vortex, surrounding it. The presence of the tip vortex significantly alters the effective angle of attack of the rotor.

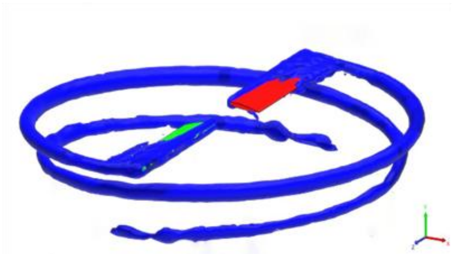

Figure 3 tip vortex core

As shown in Figure 4, it is a comparison of the numerical and experimental results of the pressure coefficient. It can be observed that the numerical results of the distribution of the pressure coefficient (C_p) agree well with the experimental values. The rotor pressure coefficient C_p can be obtained by,

$$C_p = p/(0.5\rho\omega^2 R^2) \quad (10)$$

where p is the pressure difference relative to the reference pressure.

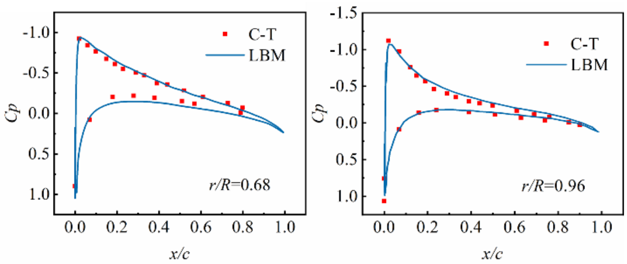

Figure 4 Pressure coefficient distribution of the Caradonna-Tung rotor

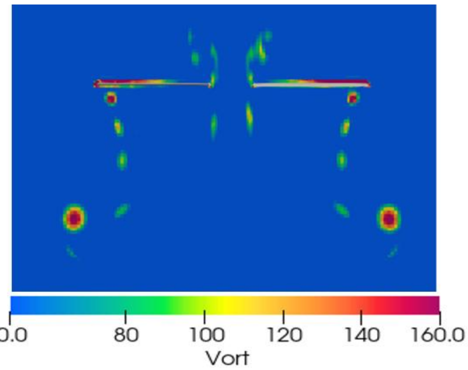

Figure 5 Vortex core iso-surface of rotor hovering state

For ease of observation, the vortex age ϕ is introduced to describe the relationship between the tip vortex detachment and the rotor's rotational revolution. The axial and radial positions of the wake vortex are compared with the experimental results of C-T rotor, as shown in the figure. It is observed that the numerical results match well with the experimental data.

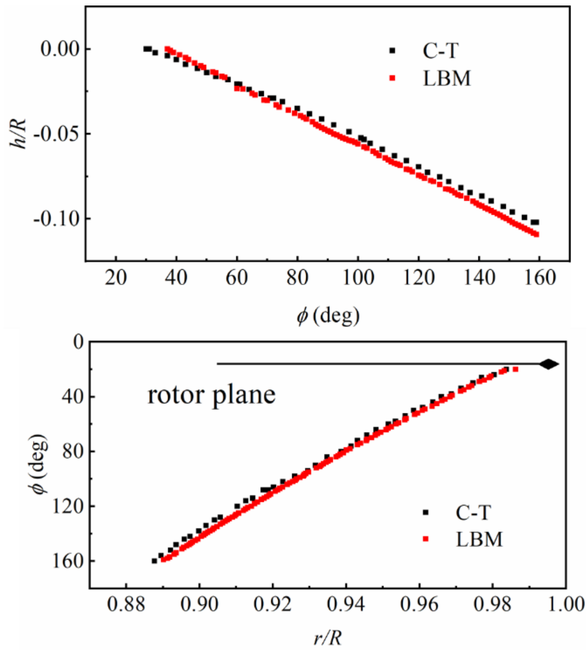

Figure 6 Position of wake vortex

4.3. Experimental validation

In this section, a single rotor/coaxial dual-rotor test platform was constructed. The experiment was conducted using a DJI-9450 rotor in a water pool, as shown in Figure 7. The rotor has a diameter of 0.239 m, which is widely used in the simulation of aerodynamics and acoustic mechanism. The parameter of the rotor has been published, which can be found in Ref. 27–29. The rotor was fixed on a rotor stack driven by a stepper motor for height adjustment above the water surface. For illumination of the downwash flow field, an Nd: YAG laser was adopted to generate a dual-pulse laser at 532 nm with frequency of 15 Hz in the experiments. The rotor speed was measured with a Hall effect sensor indexed to the motor stator, which provided a once-per-revolution synchronization signal. The sampling frequency of the data acquisition system was 100 Hz, with a sampling time of 3 seconds for each height and rotational speed. The resolution of the CCD camera used in flow visualization was 2560 pixels × 2160 pixels. A smoke generator by heating the smoke oil was used to feed smoke into the water tank, and the average diameter of the tracer smoke particles was about 5 μm.

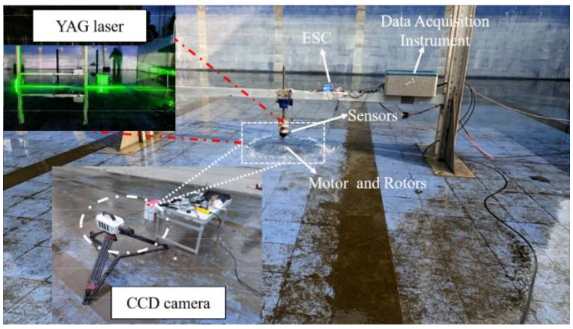

Figure 7 Experiment platform

In the experiment, three characteristic rotational speeds of 4000, 6000, and 8000 RPM at a non-dimensional height of h/R=0.2 were used to compare the variation of thrust over time. In Ref. 30, these speeds have been shown to correspond to the depression, fountain, and boiling stages, respectively. The experimental results, as shown in the Figure 8, exhibit a high degree of consistency between the numerical simulation results and the experimental data. Both demonstrate periodic fluctuations and a characteristic drop followed by recovery during the startup phase. Unfortunately, due to differences in sampling frequency and time scales during data acquisition, their dynamic characteristics cannot be made fully consistent.

Table 4 is a comparison of the simulation results and experimental results of time-averaged thrust under different rotational speed conditions. It can be seen that at low rotational speeds, the simulation error of the LBM method is less than 10%, which is an acceptable range. However, at high rotational speeds, the thrust prediction of the model shows distortion, which is due to the lack of a turbulence model capable of accurately predicting flow interference in gas-liquid coupled fields.

Table 4 Comparison of the simulation and experimental data

ω (RPM)	LBM-C_T	Exp.-C_T	e_T
4000	0.03393	0.03499	3.12%
6000	0.03639	0.03431	5.72%
8000	0.03059	0.02515	17.78%

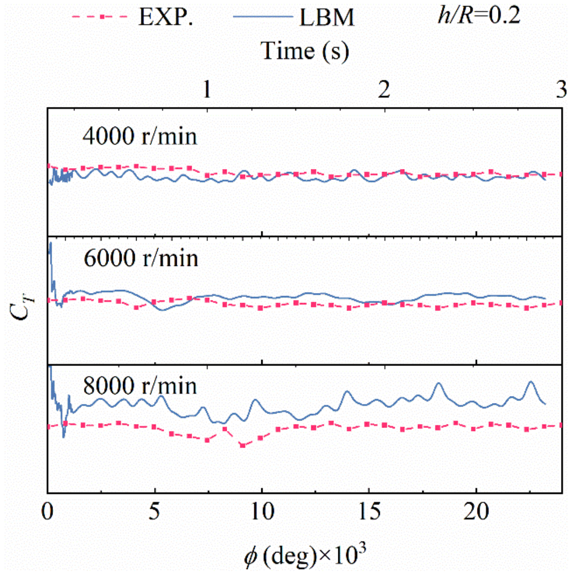

Figure 8 Comparison of experimental and numerical results at different rotational speeds

5. RESULTS AND DISCUSSION

5.1. Thrust characteristics

The comparison of rotor thrust under different non-dimensional height conditions, with the change in vortex age as the time scale, at a fixed rotational speed of 8000 RPM. In Figure 9(a), it can be observed that under the ground effect, the numerical simulation results based on the LBM method converge in a very short time, reaching a relatively stable state. The trend follows the general pattern, with thrust increasing as the non-dimensional height decreases. In Figure 9(b), it can be seen that, when far from the water surface, the thrust remains almost unchanged. As the rotor approaches the water surface, a weak ground effect posture emerges. As the rotor moves closer to the free water surface, with h/R =0.6, significant fluctuations in rotor thrust occur within the vortex age range of 3.6×10³ to 11.9×10³. As the non-dimensional height decreases further, this phenomenon gradually expands. Even though the thrust gradually recovers, it remains lower than the increase observed in the GE at the same height. In fact, in our previous studies, experiments have shown that even when the thrust of an isolated rotor recovers, it is still lower than the value observed in the absence of wall effect interference.

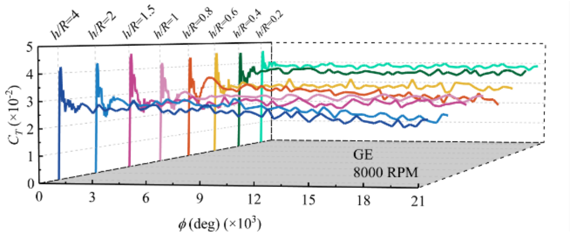

(a) Simulation results in GE

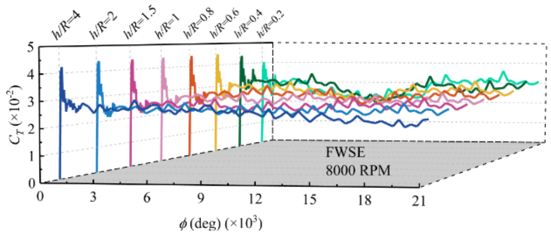

(b) Simulation results in FWSE

Figure 9 Numerical simulation results of isolated rotor at different h/R

Through the parallel dual-rotor near-water surface experiment, the results of 8000 RPM are shown in Figure 10. It was discovered that, in contrast to an isolated rotor, a smaller rotor spacing can effectively enhance the thrust of the multi-rotor. However, this also increases the degree of disorder, primarily due to the mutual interference among the rotors. Moreover, unlike the thrust coefficient in the absence of the wall effect, when there is no wall effect, the rotor thrust coefficient decreases initially and then increases as the rotor spacing diminishes. Under the influence of the wall effect, the rotor thrust increases as the rotor spacing decreases.

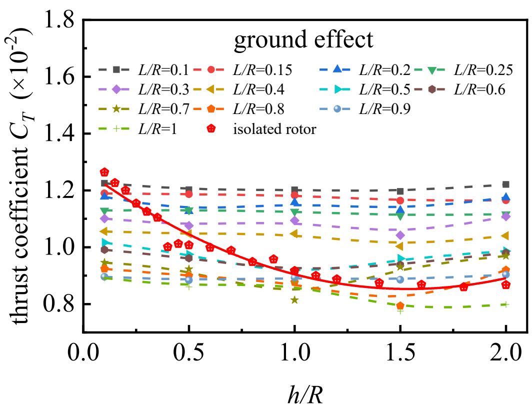

（a）Thrust coefficient in GE

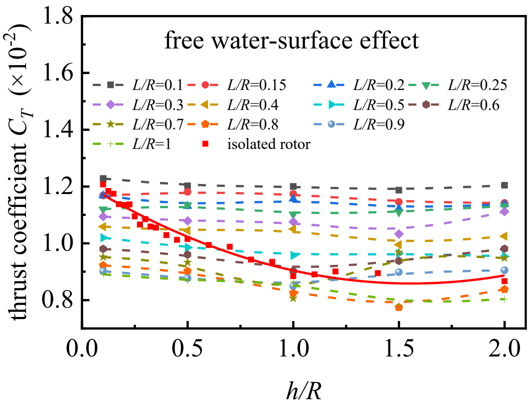

（b）Thrust coefficient in FWSE

Figure 10 Experimental results of isolated rotor and parallel dual-rotor at different rotor spacing, with ω=8000 RPM

5.2. Rotor wake characteristics

The amplitude of the liquid crown increases at the edge of the depression. Gas-liquid coupling phenomenon leads to a significantly complex physical process that contains deformation and fragmentation of liquid crown, formation of droplets, droplet motion with the rotor downwash, impact of droplets onto rotor blade, as shown in Figure 11.

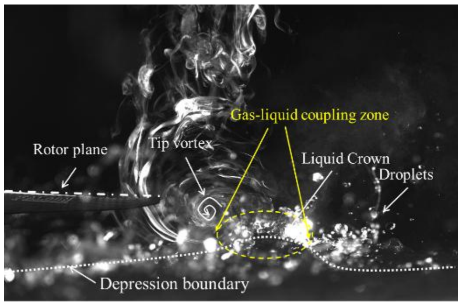

Figure 11 Rotor wake in the free water-surface effect

Figure 12 show the wake characteristics at different rotor non-dimensional rotor heights for a rotational speed of 8000 RPM. As the rotor height decreases, two distinct characteristics become evident: firstly, there is an increase in the turbulence intensity at the blade tip region; secondly, the depression boundary separating the tip vortices from the ground plane becomes thinner. Additionally, the tip vortices show more evidence of pairing, which is a typical characteristic resulting from the receding depression boundary. The latter characteristic was due to that the vortex sheets trailed from the inner parts of the blades did not have enough time and space to dissipate, so that they were rapidly coupling with the fluid crown at h/R=0.2. In contrast, at h/R=2.0, the vortex sheets had dissipated more in the downstream flow, leaving more small-scale eddies embedded in the ground flow.

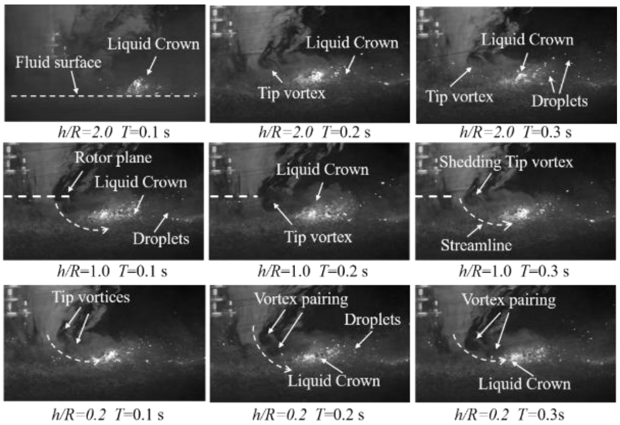

Figure 12 Flow visualization of isolated rotor

5.3. Vorticity characteristics

As shown in Figure 13, it is the vorticity contour of the rotor without the ground effect. The vorticity section surface shows a tip vortex generated at the blade tip, which follows a spiral shape that first contracts and then diffuses. This contracted wake descends slowly and remains close to the blade. Due to the tip vortex, it generates a strong induced velocity, which significantly changes the effective angle of attack of the rotor. This interference plays a dominant role in the formation of the rotor wake and directly affects the performance of the rotor.

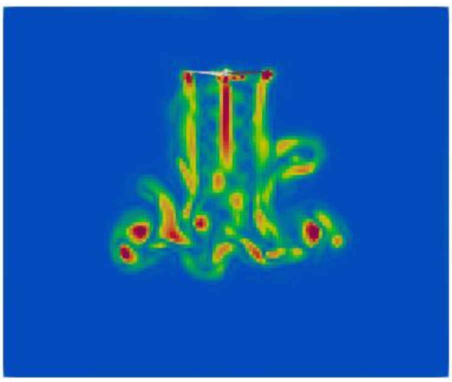

Figure 13 Vorticity distribution without ground effect

Unlike the ground effect, Figure 14 shows the transient distribution characteristics of vorticity as it dynamically changes with vortex age under the condition of a non-dimensional height of h/R=0.2 at different rotational speeds. From the figure, it can be seen that, regardless of the rotational speed, the appearance of the water surface depression affects the movement and diffusion of the vorticity. Specifically, when the rotational speed exceeds 6000 RPM, the water surface depression significantly affects the diffusion of the rotor wake vortex, altering its movement trajectory. The flow field behavior can generally be divided into three stages: First, the wake vortex behaves similarly to the ground effect, becoming trapped in the near-surface wall shear layer and diffusing outward with the jet flow. Second, under the influence of the rotor downwash, a deeper depression is formed, and a liquid crown develops at the periphery of the depression, close to the rotor plane height. The appearance of the liquid crown prevents the detached vortex from diffusing outward from the rotor plane in time, causing the rotor to enter a vortex ring state. Finally, the curvature of the depression region gradually decreases in the direction away from the rotor plane, achieving a periodic dynamic balance with the rotor downwash.

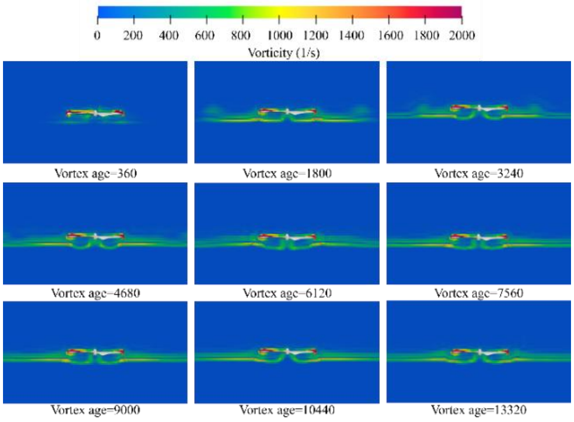

（a）Vorticity distribution with ω=4000 RPM

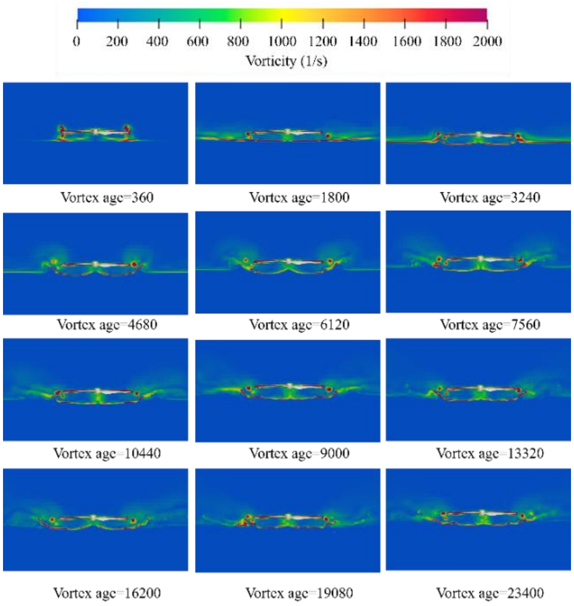

（b）Vorticity distribution with ω=6000 RPM

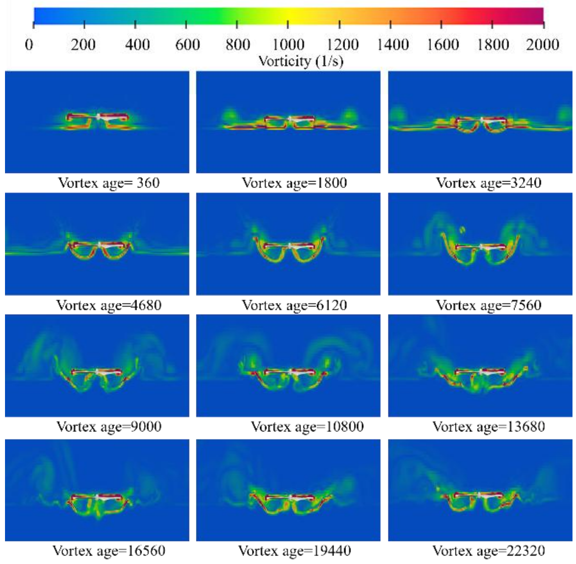

（c）Vorticity distribution with ω=8000 RPM

Figure 14 Transient vorticity distribution of the isolated rotor at different rotational speeds

Figure 15 shows the vorticity distribution of an isolated rotor at different non-dimensional heights, with a rotational speed of 8000 RPM, after the rotor flow field reaches a quasi-steady state, approximately after 40 rotor revolutions. It can be observed that, as the rotor gradually approaches the water surface, the vorticity exhibits distinctly different changes in the GE and FWSE conditions. Specifically, the rotor wake fails to diffuse in time, forming a stable wall shear layer, also known as the wall jet region, under the ground effect. This shear motion intensifies both in strength and vorticity as the rotor approaches the ground. When the vortices reach the ground, they are stretched radially, which increases their vorticity and swirl velocities. This characteristic allows these tip vortices to sustain a longer rotor revolution period. However, in the FWSE condition, this phenomenon is completely opposite. When h/R=2, the wake distribution is almost identical. As the rotor moves closer to the water surface, the stable wall shear layer is disrupted, leading to turbulence, which exacerbates the chaotic state of the flow field. When the rotor is very close to the water surface, the flow field and the water surface naturally form a quasi-steady state. In this state, the rotor wake, after passing around the liquid crown, forms a new wall shear layer along the water surface.

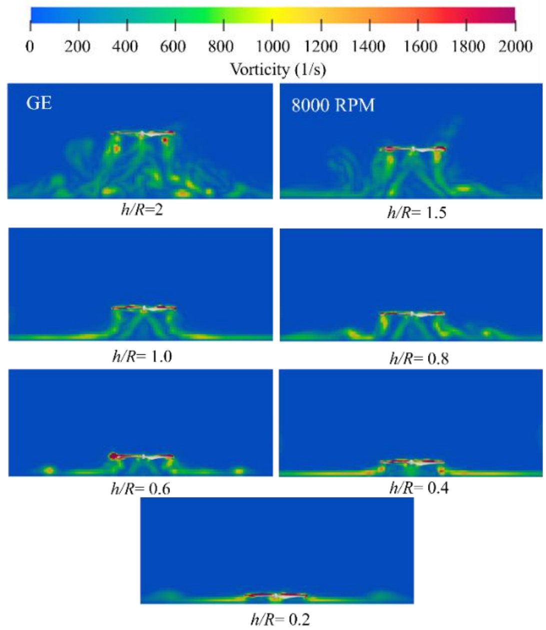

(a) Vorticity distribution of isolated rotor in GE

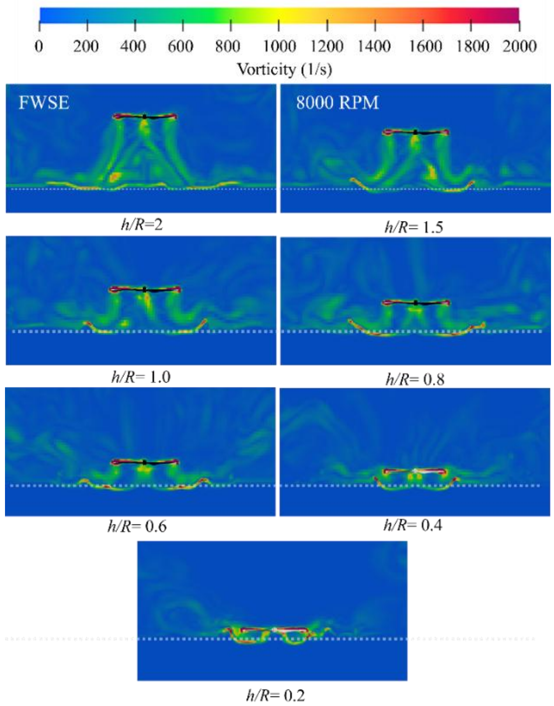

(b) Vorticity distribution of isolated rotor in FWSE

Figure 15 Vorticity distribution of the isolated rotor at different h/R with ω=8000 RPM

Figure 16 shows the vorticity distribution of the coaxial dual-rotor flow field in the FWSE condition, after the rotor flow field reaches a quasi-steady state, approximately after 40 rotor revolutions. As shown in the figure, the vorticity and rotor wake are compared at different non-dimensional heights, with a rotational speed of 8000 RPM and a rotor spacing of L=1R. It can be seen that the vorticity diffusion is completely different from that of the isolated rotor. The flow field is more complex compared to the isolated rotor, with the appearance of tip vortex interference, inter-rotor interference, and gas-liquid interference. The presence of these interference factors leads to some unique phenomena in the inter-rotor space, such as the fountain effect and reentry effect.

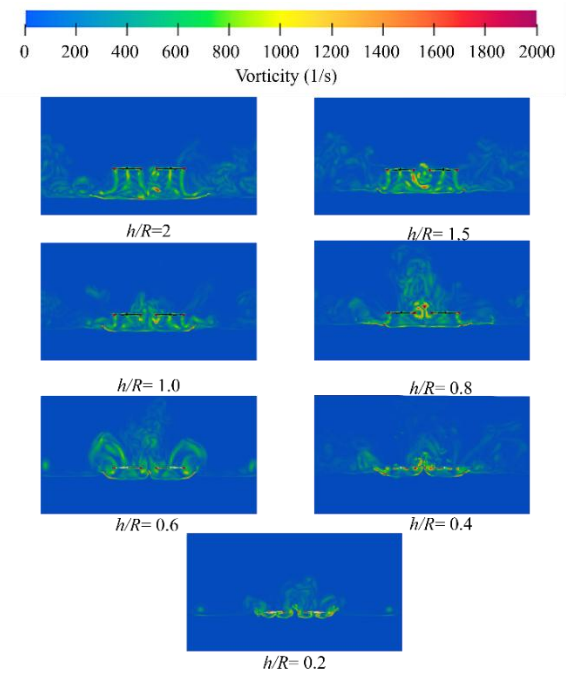

Figure 16 Vorticity distribution of the parallel dual-rotor at different h/R values with ω=8000 RPM

Figure 17 shows the variation of the rotor wake within half a rotation cycle after the rotor reaches a relatively stable state in the FWSE, approximately after 40 rotor revolutions. A comparison reveals that the influence of FWSE on the rotor wake is significant. As the non-dimensional height decreases, the rotor wake exhibits a variation pattern that is completely different from the ground effect. In the ground effect, only when h/R<0.4, the tip vortex does not have enough time and space to move and diffuse due to the avoidance of the jet flow. It is drawn into the wall jet flow, accelerating both the radial and axial diffusion of the wake. In FWSE, the detached vortex is compressed by the liquid crown, vortex sheets, and the avoidance of jet flow, causing the tip vortex to appear closer to the rotor's rotational center. Moreover, the movement of the wall jet shear layer and liquid crown intensifies the reinforcement effect on the detached vortex, which is the key cause of rotor thrust fluctuation. This phenomenon is mainly caused by the water surface depression, which acts like a rail and, under the acceleration of the wall jet flow, launches the detached tip vortex into the air. Additionally, it is worth noting from the figure that, beneath the water surface, near-wall turbulence is more easily formed, which leads to rapid diffusion of the detached vortex, preventing it from maintaining for a long time in FWSE. This turbulence effect is highly complex, shortening the duration of the detached vortex and compressing its diffusion distance.

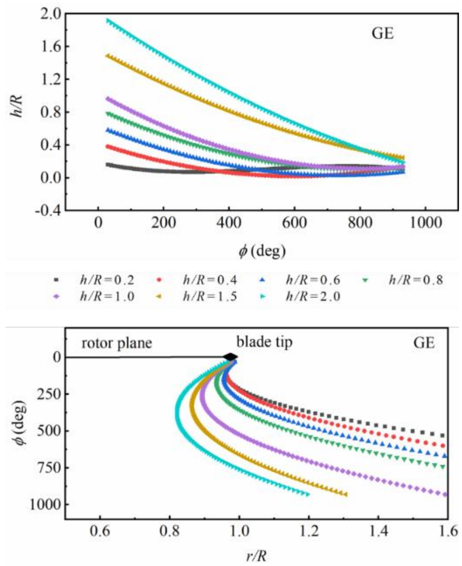

(a) Radial position variation of the wake vortex of the isolated rotor

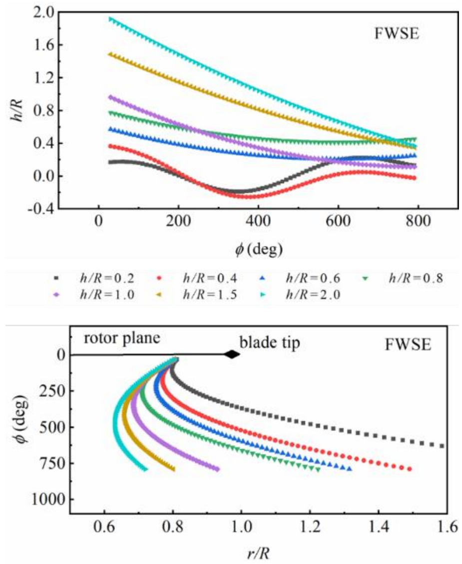

(b) Axial position variation of the wake vortex of the isolated rotor

Figure 17 Wake vortex position of the isolated rotor at ω=8000 RPM

5.4. Pressure characteristics

Figure 18 shows the pressure distribution on the upper and lower surfaces of an isolated rotor at h/R=0.2 under different rotational speed conditions. It can be observed that, as the rotational speed increases, the pressure on the lower surface of the rotor gradually increases, with the highest concentration at the blade tip.

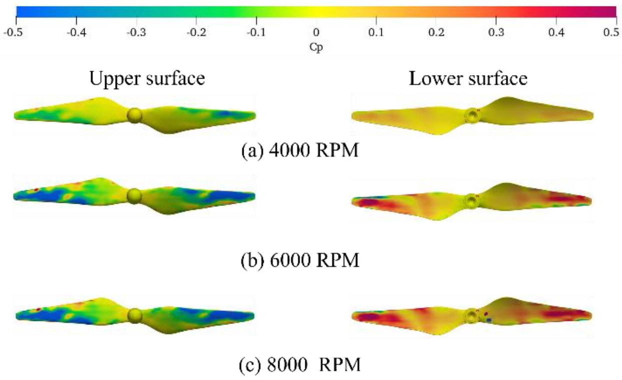

Figure 18 Surface pressure coefficient distribution of the isolated rotor at different rotational speeds

Figure 19 shows the pressure distribution on the upper and lower surfaces of an isolated rotor at ω=8000 RPM under different non-dimensional height conditions. In the comparison of the pressure distributions on the upper and lower surfaces of the rotor at different heights, the pressure distribution on the lower surface under the ground effect is more uniform, as shown in Figure 19. In FWSE, the water surface depression leads to a pressure increment on the lower surface of the rotor, concentrated at the blade tip. This phenomenon is not observed under the ground effect. The pressure distribution indicates that the rotor experiences concentrated loading, making it more prone to damage in the FWSE.

Figure 20 shows the variation of the pressure coefficient on the upper and lower surfaces of the isolated rotor along different radial sections as a function of the rotor's chord length. It can be observed that, after the FWSE reaches a relatively stable state, the pressure distribution at the blade tip under different non-dimensional heights shows significant divergence. This result seems to differ from the findings of Zhang et al (Ref. 31). In their study, the pressure distribution at the blade tip was almost identical at different heights. This discrepancy may be due to the tapered design of the DJI-9450 rotor blade.

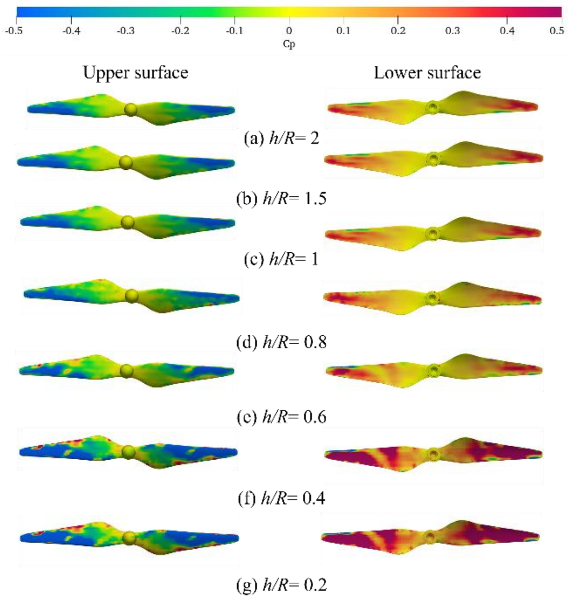

Figure 19 Surface pressure coefficient distribution of the isolated rotor at different h/R

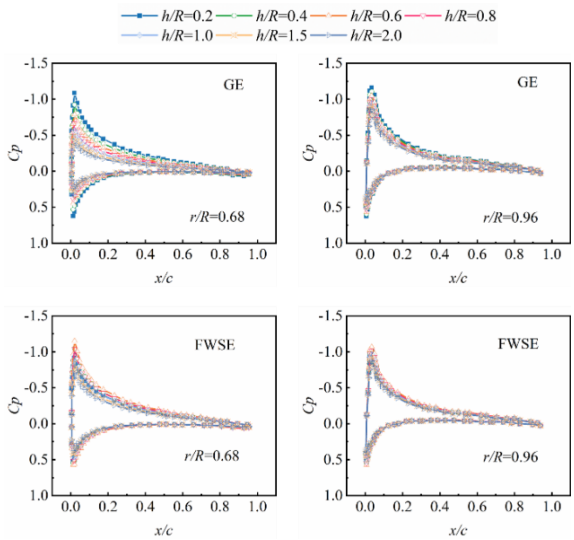

Figure 20 Pressure coefficient of the isolated rotor's cross-section

5.5. Velocity characteristics

Figure 21 shows the transient distribution characteristics of the wall jet velocity gradient as it dynamically changes with vortex age under the condition of h/R=0.2 at different rotational speeds. When the rotational speed exceeds 6000 RPM, the velocity shear layer is disrupted by the liquid crown, causing the wall jet layer near the water surface to become disordered and chaotic. As the rotational speed exceeds 8000 RPM, under the obstruction of the liquid crown, the rotor downwash gradually forms a large turbulent region in the direction of the rotor's incoming flow. This turbulence prevents the downwash from diffusing outward. The blockage effect caused by this turbulence results in an increase in the downwash velocity and a decrease in the effective angle of attack, which is a significant reason why thrust in the FWSE is lower than in the absence of the ground effect.

Additionally, a transient velocity map of the flow field in the GE condition, varying with the rotor revolution cycle, is shown in Figure 22, where h/R=0.2 and the rotor speed is 8000 RPM. From Figure 22, it can be seen that under the GE, a stable wall velocity shear layer with a velocity gradient distribution. This is because the ground is a rigid surface, and under its obstruction, a high-pressure region forms beneath the rotor, intensifying the pressure gradient and flow behavior of the wall shear layer.

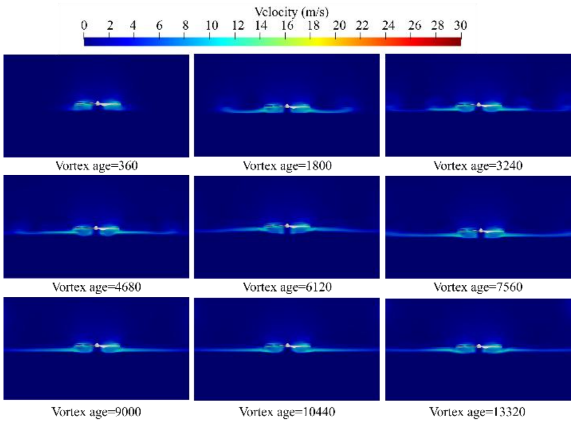

(a) Velocity field distribution of the isolated rotor in FWSE at ω=4000 RPM

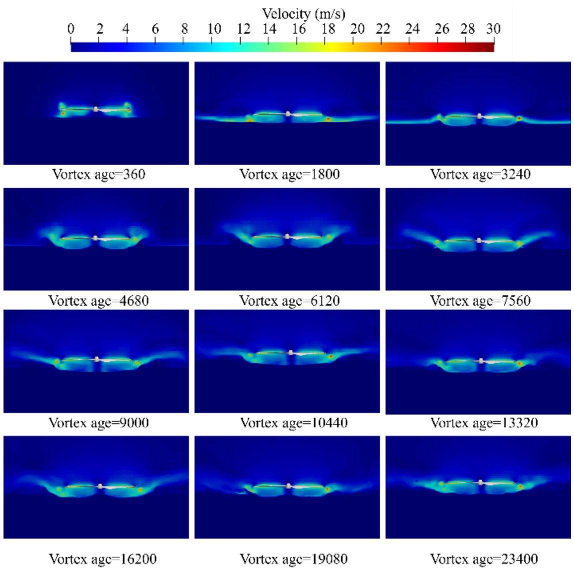

(b) Velocity field distribution of the isolated rotor in FWSE at ω=6000 RPM

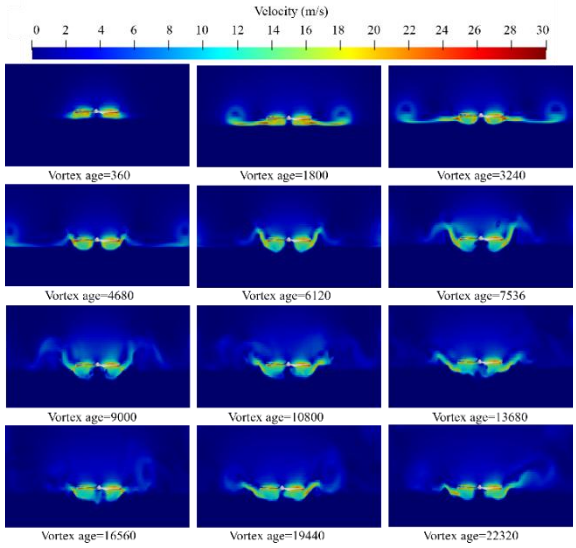

(c) Velocity field distribution of the isolated rotor in FWSE at ω=8000 RPM

Figure 21 Transient distribution of induced velocity in the flow field near the water surface for the isolated rotor

A transient velocity map of the flow field under different non-dimensional height conditions, varying with the rotor revolution cycle, is shown in Figure 23, where the rotor speed is 8000 RPM. The velocity field evolution of the rotor in FWSE at three typical heights is displayed. From the figure, it can be seen that at h/R=2, the velocity shear layer is almost unaffected by the water surface deformation. Although the water surface depression slightly alters the wake diffusion trajectory, the wall jet remains relatively stable. However, when the rotor descends to h/R=0.6, the depression caused by the downwash impact prevents the wall jet from effectively diffusing outward, creating an upward motion and even vortex ring formation within a certain time, which leads to thrust reduction. At h/R=0.2, this phenomenon is further enhanced. The velocity shear layer forms periodic turbulence, and the liquid crown's height almost encloses the rotor, preventing effective outward diffusion of the downwash flow and significantly hindering its motion. This appears to be why rotor thrust is lower than in the absence of the ground effect.

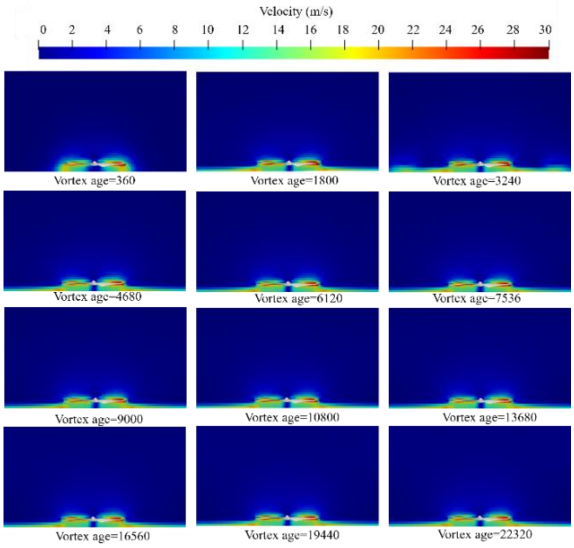

Figure 22 Transient distribution of induced velocity of the isolated rotor in GE at h/R=0.2

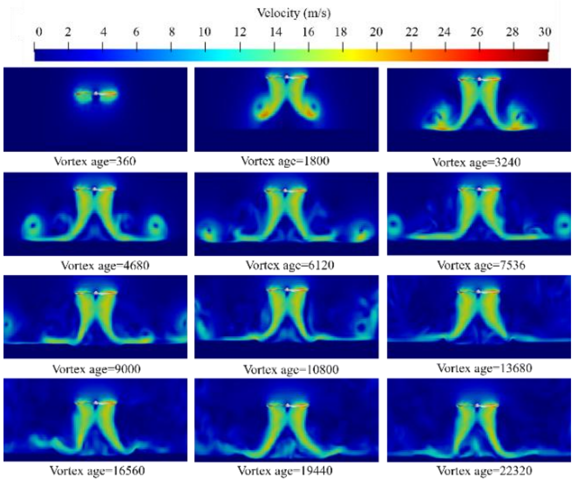

(a) induced velocity at h/R=2

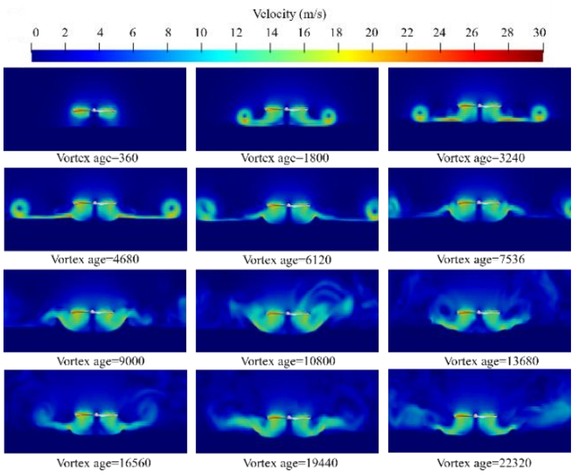

(b) induced velocity at h/R=0.6

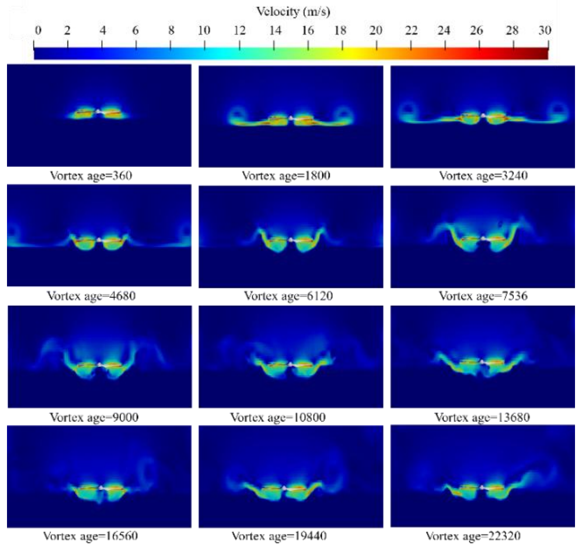

(c) induced velocity at h/R=0.2

Figure 23 Transient distribution of induced velocity of the isolated rotor in FWSE

Using an array of flow field probes, the quasi-steady induced velocity along the radial distribution of the rotor plane was measured under a rotational speed of 8000 RPM, approximately after 40 rotor revolutions, as shown in Figure 24. It can be observed that, under the ground effect, the induced velocity distribution on the rotor plane follows a certain pattern or decreases proportionally as the non-dimensional height decreases. However, in the FWSE, the variation in induced velocity shifts to an increase.

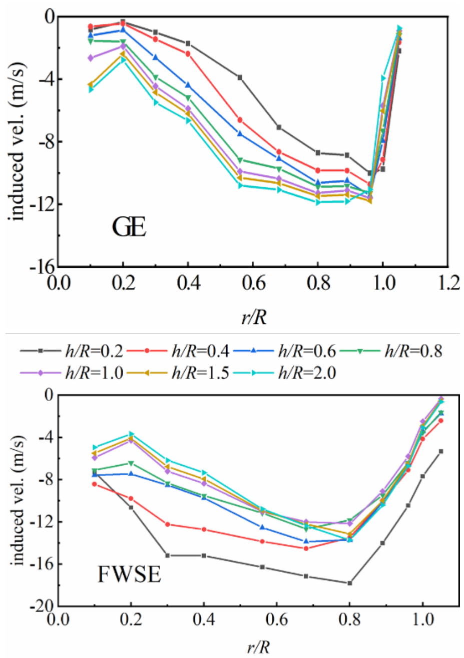

Figure 24 Radial variation of induced velocity of the isolated rotor

In Figure 25, the induced velocity distribution pattern on the rotor plane of the coaxial dual-rotor system can be observed. The variation in induced velocity on the outer side of the rotor axis follows a pattern similar to that observed under the water surface effect. However, the induced velocity variation on the inner side of the rotor axis is more similar to the ground effect. This explains why the coaxial dual-rotor system can effectively mitigate the negative effects of the free water surface. However, this also exacerbates the non-uniformity and asymmetry of the aerodynamic force distribution on the rotor plane, leading to larger concentrated stresses and aerodynamic moments at the root of the blades. In fact, if the rotor system being studied is of larger size, this could result in flapping oscillations and unpredictable rotor moments.

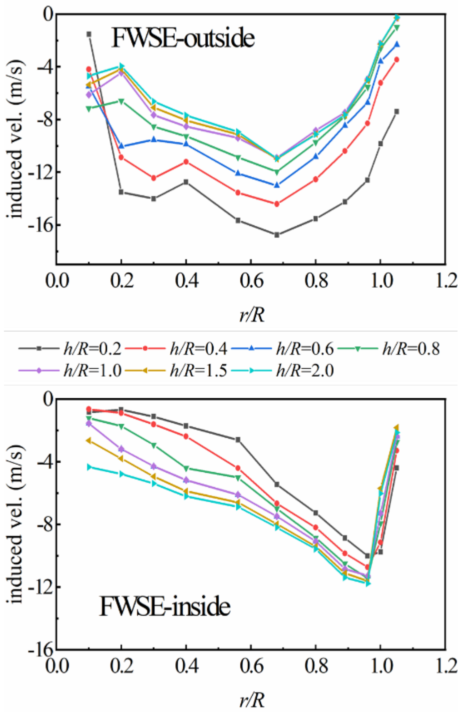

Figure 25 Radial variation of induced velocity of the parallel dual-rotor

6. CONCLUSIONS

This paper presents a numerical simulation method combining the Lattice-Boltzmann method (LBM) and wall-model large-eddy simulation (WM-LES) with the Shan-Chen multiphase flow model to investigate the aerodynamic characteristics of rotors near the water surface. The study focuses on the behavior of rotorcraft in the ground effect and free water surface effect, analyzing the impact of varying operating conditions on induced velocity, pressure distribution, and vortex dynamics in both isolated and parallel dual-rotors.

The results show that induced velocity decreases as non-dimensional height reduces in GE, consistent with conventional rotorcraft behavior. However, in FWSE, induced velocity increases, particularly as the rotor nears the water surface. This shift is due to the interaction between the rotor wake and water surface depression, introducing complexities like vortex ring formation and wall jet behavior, which do not occur in ground effect scenarios.

The study further reveals the significant influence of the water surface on rotor thrust distribution. In FWSE, pressure at the blade tip increases, leading to more concentrated loading on the rotor, which may elevate the risk of rotor damage, especially in larger rotors. The parallel dual-rotor system mitigates some negative effects by reducing asymmetry and non-uniformity in load distribution compared to isolated rotors. However, it introduces complex rotor interactions, resulting in increased stress and aerodynamic moments, particularly at the blade tip, which could lead to unpredictable rotor moments and flapping oscillations.

This study enhances the understanding of rotorcraft aerodynamics in complex fluid environments and provides insights for improving performance in aerial-aquatic applications.

Author contact:

Qi ZHAN qizhan@nuaa.edu.cn

Yumin YANG yuminyang@nuaa.edu.cn

Shuai ZHAO shuaizhao@nuaa.edu.cn

Yousong XU xuyousong@nuaa.edu.cn

Xiao WANG x.wang@nuaa.edu.cn

Junhui HU ejhhu@nuaa.edu.cn

7. ACKNOWLEDGMENTS

The authors thank the National Natural Science Foundation of China (No. 12272169) and the Postgraduate Research & Practice Innovation Program of Jiangsu Province (No. KYCX24_0532) for the financial support.

REFERENCES

1. G. Yao, Y. Li, H. Zhang, Y. Jiang, T. Wang, F. Sun, and X. Yang, Review of Hybrid Aquatic-

Aerial Vehicle (HAAV): Classifications, Current Status, Applications, Challenges and Technology Perspectives, *Progress in Aerospace Sciences*, 2023, 139, p 100902, doi:10.1016/j.paerosci.2023.100902.

2. Z. Zeng, C. Lyu, Y. Bi, Y. Jin, D. Lu, and L. Lian, Review of Hybrid Aerial Underwater Vehicle: Cross-Domain Mobility and Transitions Control, *Ocean Engineering*, 2022, 248, p 110840, doi:10.1016/j.oceaneng.2022.110840.
3. M. Hassanalian and A. Abdelkefi, Classifications, Applications, and Design Challenges of Drones: A Review, *Prog. Aerosp. Sci.*, 2017, 91, p 99–131, doi:10.1016/j.paerosci.2017.04.003.
4. Y. Sun, Y. Xu, H. Shen, J. Liu, Y. Gao, Q. Zhao, and A. Ji, Analysis of Water Surface Effects during the Water-Exit Process of the Vector Bi-Rotor Aerial-Aquatic Vehicle, *Aerospace Science and Technology*, 2025, 164, p 110404, doi:10.1016/j.ast.2025.110404.
5. A. Villegas, V. Mishkevich, Y. Gulak, and F.J. Diez, Analysis of Key Elements to Evaluate the Performance of a Multirotor Unmanned Aerial–Aquatic Vehicle, *Aerospace Science and Technology*, 2017, 70, p 412–418, doi:10.1016/j.ast.2017.07.046.
6. Y. Bi, D. Lu, Z. Zeng, and L. Lian, Dynamics and Control of Hybrid Aerial Underwater Vehicle Subject to Disturbances, *Ocean Eng.*, 2022, 250, p 110933, doi:10.1016/j.oceaneng.2022.110933.
7. X.-Z. Bai, Z. Zhang, W.-H. Wu, X. Wang, Q. Zhan, D.-X. Zhang, and L. Yu, Fluid Dynamics of Interacting Rotor Wake with a Water Surface, *Drones*, 2024, 8(9), p 469, doi:10.3390/drones8090469.
8. J. Wei, Y.B. Sha, X.Y. Hu, J.Y. Yao, and Y.L. Chen, Aerodynamic Numerical Simulation Analysis of Water-Air Two-Phase Flow in Trans-Medium Aircraft, *Drones-Basel*, 2022, 6(9), p 236, doi:10.3390/drones6090236.
9. X. Bai, M. Lu, Q. Zhan, Y. Wang, D. Zhang, X. Wang, and W. Wu, Review of the Near-Water Effect of Rotors in Cross-Media Vehicles, *Drones*, 2025, 9(3), p 195, doi:10.3390/drones9030195.
10. C.W. Hirt and B.D. Nichols, Volume of Fluid (VOF) Method for the Dynamics of Free Boundaries, *Journal of Computational Physics*, 1981, 39(1), p 201–225, doi:10.1016/0021-9991(81)90145-5.
11. L. Chen, Q. Kang, Y. Mu, Y.-L. He, and W.-Q. Tao, A Critical Review of the Pseudopotential Multiphase Lattice Boltzmann Model: Methods and Applications, *International Journal of Heat and Mass Transfer*, 2014, 76, p 210–236, doi:10.1016/j.ijheatmasstransfer.2014.04.032.
12. H. Wang, X. Yuan, H. Liang, Z. Chai, and B. Shi, A Brief Review of the Phase-Field-Based Lattice Boltzmann Method for Multiphase Flows, *Capillarity*, 2019, 2(3), p 33–52, doi:10.26804/capi.2019.03.01.
13. Q. Li, K.H. Luo, Q.J. Kang, Y.L. He, Q. Chen, and Q. Liu, Lattice Boltzmann Methods for Multiphase Flow and Phase-Change Heat Transfer, *Progress in Energy and Combustion Science*, 2016, 52, p 62–105, doi:10.1016/j.pecs.2015.10.001.
14. Sudhakar Thippavathini, T. Sudhakar, T. Sudhakar, Arup Kumar Das, and A.K. Das, Evolution of Multiphase Lattice Boltzmann Method: A Review, *Journal of The Institution of Engineers : Series C*, 2020, 101(4), p 711–719, doi:10.1007/s40032-020-00600-8.
15. D.H. Rothman and J.M. Keller, Immiscible Cellular-Automaton Fluids, *Journal of Statistical Physics*, Springer, 1988, 52(3), p 1119–1127, doi:10.1007/BF01019743.
16. M.R. Swift, W.R. Osborn, and J.M. Yeomans, Lattice Boltzmann Simulation of Nonideal Fluids, *Phys. Rev. Lett.*, American Physical Society, 1995, 75(5), p 830–833, doi:10.1103/PhysRevLett.75.830.
17. X. He, S. Chen, and R. Zhang, A Lattice Boltzmann Scheme for Incompressible Multiphase Flow and Its Application in Simulation of Rayleigh–Taylor Instability, *Journal of Computational Physics*, 1999, 152(2), p 642–663, doi:10.1006/jcph.1999.6257.
18. X. Shan and H. Chen, Simulation of Nonideal Gases and Liquid-Gas Phase Transitions by the Lattice Boltzmann Equation, *Phys Rev E Stat Phys Plasmas Fluids Relat Interdiscip Topics*, 1994, 49(4), p 2941–2948, doi:10.1103/physreve.49.2941.
19. U. Frisch, B. Hasslacher, and Y. Pomeau, Lattice-Gas Automata for the Navier-Stokes Equation, *Phys. Rev. Lett.*, American Physical Society, 1986, 56(14), p 1505–1508, doi:10.1103/PhysRevLett.56.1505.
20. D. Zhang, K. Papadikis, and S. Gu, Three-Dimensional Multi-Relaxation Time Lattice-Boltzmann Model for the Drop Impact on a Dry Surface at Large Density Ratio, *International Journal of Multiphase Flow*, 2014, 64, p 11–18, doi:10.1016/j.ijmultiphaseflow.2014.04.005.
21. M. Haussmann, F. Ries, J.B. Jeppener-Haltenhoff, Y. Li, M. Schmidt, C. Welch, L. Illmann, B. Böhm, H. Nirschl, M.J. Krause, and A. Sadiki, Evaluation of a Near-Wall-Modeled Large Eddy Lattice Boltzmann Method for the Analysis of Complex Flows Relevant to IC Engines, *Computation*, Multidisciplinary Digital

Publishing Institute, 2020, 8(2), p 43, doi:10.3390/computation8020043.
22. T.-H. Shih, L.A. Povinelli, N.-S. Liu, M.G. Potapczuk, and J.L. Lumley, “A Generalized Wall Function,” 1999, https://ntrs.nasa.gov/citations/19990081113. Accessed 4 July 2025.
23. P. Yuan and L. Schaefer, Equations of State in a Lattice Boltzmann Model, *Physics of Fluids*, 2006, 18(4), p 042101, doi:10.1063/1.2187070.
24. M.R. Kamali and H.E.A. Van den Akker, Simulating Gas–Liquid Flows by Means of a Pseudopotential Lattice Boltzmann Method, *Ind. Eng. Chem. Res.*, American Chemical Society, 2013, 52(33), p 11365–11377, doi:10.1021/ie303356u.
25. M.J. Krause, S. Avis, H. Kusumaatmaja, D. Dapalo, M. Gaedtke, and N. Hafen, “OpenLB Release 1.4: Open Source Lattice Boltzmann Code,” 2020, https://doi.org/10.5281/zenodo.4279263.
26. F.X. Caradonna and C. Tung, “Experimental and Analytical Studies of a Model Helicopter Rotor in Hover,” (Bristol), 1981, https://ntrs.nasa.gov/citations/19820004169. Accessed 20 February 2025.
27. N.S. Zawodny, D.D. Boyd, and C.L. Burley, “Acoustic Characterization and Prediction of Representative, Small-Scale Rotary-Wing Unmanned Aircraft System Components,” (West Palm Beach, FL), 2016, https://ntrs.nasa.gov/citations/20160009054. Accessed 29 May 2025.
28. T. Suresh, O. Szulc, and P. Flaszynski, Aeroacoustic Analysis Based on FW–H Analogy to Predict Low-Frequency in-Plane Harmonic Noise of a Helicopter Rotor in Hover, Archives of Mechanics, 2022, doi:10.24423/AOM.3999.
29. C.S. Thurman, J.D. Baeder, and N.S. Zawodny, “Computational Prediction of Broadband Noise from a Representative Small Unmanned Aerial System Rotor,” The Vertical Flight Society, 2020, doi:10.4050/F-0076-2020-16492.
30. Qi ZHAN, Xiao WANG, Junhui HU, Xingzhi BAI, and Pierangelo MASARATI, Aerodynamic Modeling and Analysis of Aerial-Aquatic Rotorcraft Performance near and Crossing the Air-Water Interface, *Chinese Journal of Aeronautics*, 2025, doi:10.1016/j.cja.2025.103511.
31. M. Zhang, W. Duan, W. Shao, and J. Liu, Comparison of Rotor Hovering Aerodynamic Performance in Free-Surface and Ground Effects Using Numerical Methods, *Physics of Fluids*, 2024, 36(10), p 106107, doi:10.1063/5.0222515.